

Numerical study of spin-polarized deuterium-tritium fuel persistence in inertial confinement fusion implosions

Ronghao Hu^{1,2}, Hao Zhou^{1,2}, Zhihao Tao^{1,2}, Zhihao Zhang^{1,2}, Meng Lv^{1,2,*}, Shiyang Zou³, and Yongkun Ding³

¹College of Physics, Sichuan University, Chengdu 610065, People's Republic of China

²Key Laboratory of High Energy Density Physics and Technology, Ministry of Education, Sichuan University, Chengdu 610064, People's Republic of China

³Institute of Applied Physics and Computational Mathematics, Beijing 100094, People's Republic of China



(Received 22 February 2022; accepted 10 August 2023; published 18 August 2023)

The persistence of spin-polarized fuels is a crucial problem for polarized magnetic and inertial confinement fusion (ICF). The depolarizations of polarized deuterium-tritium (DT) fuels in indirectly driven ICF implosions are investigated with three-dimensional spin transport hydrodynamics simulations. The spin transport equations for deuterons and tritons are derived with the density matrix formalism, which are used to investigate the evolutions of spin eigenstate distributions of DT fuel. The depolarization of DT ions by strong self-generated magnetic fields and the mixings of DT ions with different spin states can be captured by the spin transport equation. The simulation results show that triton polarizations are sensitive to large scale magnetic fields generated by polar mode asymmetries. It is also found that the depolarization of tritons can be reduced by an optimized spin alignment of the polarized fuel. The methods and results can be used to optimize the design of polarized fusion targets and interpret polarized fusion experiments.

DOI: [10.1103/PhysRevResearch.5.033115](https://doi.org/10.1103/PhysRevResearch.5.033115)

I. INTRODUCTION

The persistence of spin-polarized fuels in magnetic and inertial confinement fusion (ICF) plasmas is a key problem that has been discussed for many years [1–7]. The deuterium-tritium (DT) fuels are used for fusion ignitions because the cross sections for DT reactions are larger over other reactions at keV energies. The fusion cross sections can be further increased by about 50% when the spins of DT ions are parallel [1,2,8]. This makes polarized DT fuels very attractive for achieving fusion ignition and high gain. In ICF, the fusion ignition has been reached with 2.05 MJ laser energy input and 3.15 MJ neutron energy output, showing an energy gain of 1.54 [9]. But due to shot-to-shot variations, the ignitions are still not very stable and the energy gains are also small [10,11]. Numerical simulations show that the hot-spot temperature and areal density required for ignition can both be reduced by about 15% for a fully polarized DT fuel [12]. The required driver energy can also be reduced for a given gain and capsule design [13]. Polarized deuterium and tritium atoms with high polarization can be produced by the atomic beam source [14,15]. The nuclear polarization of atoms can be preserved during recombination to form “hyperpolarized molecules” [16]. If the polarized gas can be filled into the ICF

capsule without severe depolarization, then the most significant question remaining is whether the polarized fuel could survive in the ICF implosion and enhance the fusion burn. Theoretical estimates and numerical simulations show that the depolarizations caused by particle collisions are negligible [3,17]. The major depolarization mechanism of polarized DT fuel during ICF implosion is magnetic field induced depolarization [18]. Hydrodynamic instabilities, like Rayleigh-Taylor instability (RTI) and Richtmyer-Meshkov instability, can generate intense magnetic fields due to the Biermann battery effect [19–21]. The periods of the Larmor precession for DT nuclei in strong magnetic fields are close to the ICF confinement time, so the depolarization by magnetic fields cannot be neglected. However, previous simulations of polarized ICF implosions did not include the depolarizations by magnetic fields due to the lack of a self-consistent simulation method [12,13,17]. The depolarization and spin transport process can be simulated using particle-based methods [22–25], hydrodynamic methods [26], or hybrid methods [18]. Hydrodynamics simulations are widely used to interpret ICF experiments [27], but conventional hydrodynamics codes do not include spin transport simulation. For spin polarized fusion, the probability distributions for spin eigenstates of DT are necessary to obtain the fusion cross sections and neutron yields. The previously proposed spin transport equations using the vector polarizations are not enough for spin-1 particles, whose tensor polarizations are also needed to obtain the probability distribution for spin eigenstates [26,28–30].

In this paper, we investigate the persistence of DT fuels in indirectly driven ICF implosions with three-dimensional (3D) hydrodynamics simulations. In Sec. II, the unified spin transport equations for spin- $\frac{1}{2}$ (T) and spin-1(D) particles are

*Corresponding author: lvmengphys@scu.edu.cn

Published by the American Physical Society under the terms of the [Creative Commons Attribution 4.0 International license](https://creativecommons.org/licenses/by/4.0/). Further distribution of this work must maintain attribution to the author(s) and the published article's title, journal citation, and DOI.

obtained with the density matrix formalism. The spin transport hydrodynamics (STHD) simulation method [31] is used to solve the radiation hydrodynamics equations, magnetic induction equation, spin transport equations, and fusion rate equation self-consistently. In Sec. III, the 3D STHD simulations results are analyzed. The triton polarization, deuteron vector, and tensor polarizations are obtained from the simulations. The neutron yields and neutron angular distributions from the simulations can be used to interpret the polarized ICF experiments, as *in situ* measurements of fuel polarizations are very difficult.

II. METHOD

A. Spin transport equation in density matrix formalism

To obtain the spin transport equation for DT nuclei, we start from the single particle Schrödinger equation

$$i\hbar \frac{\partial}{\partial t} \Psi_\alpha = \hat{H} \Psi_\alpha, \quad (1)$$

with the Hamiltonian \hat{H} ,

$$\hat{H} = -\frac{\hbar^2}{2m} \nabla^2 - \hat{\boldsymbol{\mu}} \cdot \mathbf{B}, \quad (2)$$

where α denotes the α th particle, m is the particle mass, $\hat{\boldsymbol{\mu}} = \gamma \hat{s}$ is the magnetic moment, γ is the gyromagnetic ratio, \hat{s} is spin operator and \mathbf{B} is the magnetic field. Here the spin orbit and spin-spin interaction terms in the Hamiltonian are neglected because the interaction cross sections are relatively small. The collisional depolarization caused by these interactions is estimated to be neglectable in ICF implosions [3,17]. The wave function Ψ_α can be decomposed as [26]

$$\Psi_\alpha = \sqrt{n_\alpha} \exp(iS_\alpha/\hbar) \varphi_\alpha, \quad (3)$$

where $n_\alpha(\mathbf{r}, t)$, $S_\alpha(\mathbf{r}, t)$ are real functions. φ_α is the 2-spinor for spin- $\frac{1}{2}$ particle or the 3-spinor for spin-1 particle. The single particle density $n_\alpha = \Psi_\alpha^\dagger \Psi_\alpha$ satisfies

$$\begin{aligned} \frac{\partial n_\alpha}{\partial t} &= \left(\frac{\hat{H} \Psi_\alpha}{i\hbar} \right)^\dagger \Psi_\alpha + \Psi_\alpha^\dagger \left(\frac{\hat{H} \Psi_\alpha}{i\hbar} \right) \\ &= \nabla \cdot \left[\left(\frac{i\hbar}{2m} \nabla \Psi_\alpha \right)^\dagger \Psi_\alpha + \Psi_\alpha^\dagger \left(\frac{i\hbar}{2m} \nabla \Psi_\alpha \right) \right] \\ &\quad + \left[\left(\frac{-\hat{\boldsymbol{\mu}} \cdot \mathbf{B}}{i\hbar} \Psi_\alpha \right)^\dagger \Psi_\alpha + \Psi_\alpha^\dagger \left(\frac{-\hat{\boldsymbol{\mu}} \cdot \mathbf{B}}{i\hbar} \Psi_\alpha \right) \right]. \end{aligned} \quad (4)$$

As the components of spin operator \hat{s} are Hermitian and $\hat{\boldsymbol{\mu}} \cdot \mathbf{B}$ is also Hermitian, the second term on the right-hand side of Eq. (4) is zero. The current density is defined as $\mathbf{J}_\alpha = \left(\frac{-i\hbar}{2m} \nabla \Psi_\alpha \right)^\dagger \Psi_\alpha + \Psi_\alpha^\dagger \left(\frac{-i\hbar}{2m} \nabla \Psi_\alpha \right)$, and then the equation of continuity can be obtained

$$\frac{\partial n_\alpha}{\partial t} + \nabla \cdot \mathbf{J}_\alpha = 0. \quad (5)$$

The velocity of the particle can be defined as [26]

$$\mathbf{v}_\alpha = \mathbf{J}_\alpha / n_\alpha = \frac{\nabla S_\alpha - i\hbar \varphi_\alpha^\dagger \nabla \varphi_\alpha}{m}. \quad (6)$$

The density matrix is defined as $\hat{\eta}_\alpha = \frac{\Psi_\alpha \otimes \Psi_\alpha^\dagger}{n_\alpha}$, where \otimes denotes the tensor product. The evolution of density matrix can be written as

$$\begin{aligned} \frac{\partial n_\alpha \hat{\eta}_\alpha}{\partial t} + \nabla \cdot (n_\alpha \hat{\eta}_\alpha \mathbf{v}_\alpha) &= \frac{i}{\hbar} [\hat{\boldsymbol{\mu}} \cdot \mathbf{B}, n_\alpha \hat{\eta}_\alpha] \\ &\quad + \frac{i\hbar}{2m} \nabla \cdot [\nabla \hat{\eta}_\alpha, n_\alpha \hat{\eta}_\alpha], \end{aligned} \quad (7)$$

where $[\hat{A}, \hat{B}] = \hat{A}\hat{B} - \hat{B}\hat{A}$ is the commutator.

The total density of a particle specie is $n = \sum_\alpha n_\alpha$. The density matrix of a particle specie is defined as $\hat{\eta} = \sum_\alpha n_\alpha \hat{\eta}_\alpha / n$ and the fluid velocity is $\mathbf{v} = \sum_\alpha n_\alpha \mathbf{v}_\alpha / n$. With these definitions, we can obtain the spin transport equation for a particle specie as

$$\frac{\partial n \hat{\eta}}{\partial t} + \nabla \cdot (n \hat{\eta} \mathbf{v}) = \frac{i}{\hbar} [\hat{\boldsymbol{\mu}} \cdot \mathbf{B}, n \hat{\eta}] - \nabla \cdot \hat{\mathbf{K}} + \nabla \cdot \hat{\mathbf{Q}}, \quad (8)$$

where $\hat{\mathbf{K}} = \sum_\alpha n_\alpha (\hat{\eta}_\alpha - \hat{\eta})(\mathbf{v}_\alpha - \mathbf{v})$ is the thermal-spin coupling, $\hat{\mathbf{Q}} = \frac{i\hbar}{2m} \sum_\alpha [\nabla \hat{\eta}_\alpha, n_\alpha \hat{\eta}_\alpha]$ is the nonlinear spin fluid contribution. The spin transport equation (8) still contains the explicit sum over all particles, and further statistical relations are needed to close the system. If the spin distribution and thermal distribution are not correlated, the thermal-spin coupling $\hat{\mathbf{K}} = 0$. And if the typical fluid length scale $L \gg \lambda_{th}$, where λ_{th} is the thermal de Broglie wave length, the nonlinear spin fluid contribution $\hat{\mathbf{Q}}$ can be neglected.

B. Spin transport hydrodynamics simulation

The STHD simulation method modifies the radiation hydrodynamics simulation method to include the spin transport equations. The simulations are explicitly advanced in time using the forward Euler method. In each time step, the hydrodynamics equations are first solved with Harten-Lax-van Leer (HLL) Riemann solver [32],

$$\frac{\partial \rho}{\partial t} + \nabla \cdot (\rho \mathbf{v}) = 0, \quad (9)$$

$$\frac{\partial \rho \mathbf{v}}{\partial t} + \nabla \cdot (\rho \mathbf{v} \otimes \mathbf{v}) + \nabla p = 0, \quad (10)$$

$$\frac{\partial \rho E}{\partial t} + \nabla \cdot [(\rho E + p) \mathbf{v}] = 0, \quad (11)$$

$$\frac{\partial \rho e_i}{\partial t} + \nabla \cdot (\rho e_i \mathbf{v}) + p_i \nabla \cdot \mathbf{v} = 0, \quad (12)$$

$$\frac{\partial \rho e_e}{\partial t} + \nabla \cdot (\rho e_e \mathbf{v}) + p_e \nabla \cdot \mathbf{v} = 0, \quad (13)$$

where ρ is the mass density, \mathbf{v} is fluid velocity, $p = p_i + p_e$ is the pressure, p_i is the ion pressure, p_e is the electron pressure, $E = \mathbf{v}^2/2 + e_i + e_e$ is the total energy per unit mass, e_i is the ion specific internal energy, and e_e is the electron specific internal energy. The pressures and specific internal energies of ions and electrons are calculated using the equations of states (EOS). Two materials are included in the simulation for the fuels and ablaters, and the equation of the fuel mass fraction f is solved,

$$\frac{\partial \rho f}{\partial t} + \nabla \cdot (\rho f \mathbf{v}) = 0. \quad (14)$$

Then the magnetic induction equation with Biermann battery term is solved [18],

$$\frac{\partial \mathbf{B}}{\partial t} - \nabla \times (\mathbf{v} \times \mathbf{B}) = \nabla \times \left(\frac{\nabla p_e}{n_e e} \right), \quad (15)$$

where \mathbf{B} is the magnetic field, n_e is electron number density, and e is elementary charge. The energy exchange between electrons and ions, and electron anisotropic thermal conduction are considered,

$$\rho \frac{\partial e_i}{\partial t} = \rho K_{ei}(T_e - T_i), \quad (16)$$

$$\rho \frac{\partial e_e}{\partial t} = \rho K_{ei}(T_i - T_e) + \nabla \cdot [\kappa_{\parallel}(\mathbf{b} \cdot \nabla T_e)\mathbf{b} + \kappa_{\perp}\mathbf{b} \times (\nabla T_e \times \mathbf{b}) + \kappa_{\wedge}\mathbf{b} \times \nabla T_e], \quad (17)$$

where K_{ei} is the coefficient for energy exchange between electrons and ions [33] and $\kappa_{\parallel}, \kappa_{\perp}, \kappa_{\wedge}$ are anisotropic thermal conductivities of electrons [34]. Steady-state radiation diffusion equations are used to model the radiation transport,

$$\nabla \cdot \left(\frac{1}{3\sigma_{t,g}} \nabla u_g \right) = \sigma_{a,g} u_g - \sigma_{e,g} U_g^P, \quad (18)$$

$$\frac{\rho}{c} \frac{\partial e_e}{\partial t} = \sum_g (\sigma_{a,g} u_g - \sigma_{e,g} U_g^P). \quad (19)$$

The radiation spectra is discretized into multiple frequency groups, u_g is the energy density for group g , $\sigma_{t,g}$ is the transport opacity, $\sigma_{a,g}$ is the absorption opacity, $\sigma_{e,g}$ is the emission opacity, c is the light velocity, and U_g^P is the Planckian energy density. The spin transport equations for DT ions can be written as

$$\frac{\partial \rho f \hat{\eta}}{\partial t} + \nabla \cdot (\rho f \hat{\eta} \mathbf{v}) = \frac{i}{\hbar} [\hat{\boldsymbol{\mu}} \cdot \mathbf{B}, \rho f \hat{\eta}]. \quad (20)$$

Using operator splitting, Eq. (20) is split into two equations:

$$\frac{\partial \rho f \hat{\eta}}{\partial t} + \nabla \cdot (\rho f \hat{\eta} \mathbf{v}) = 0, \quad (21)$$

$$\frac{\partial \hat{\eta}}{\partial t} = \frac{i}{\hbar} [\hat{\boldsymbol{\mu}} \cdot \mathbf{B}, \hat{\eta}]. \quad (22)$$

Equation (21) is solved using the HLL fluxes $\rho \mathbf{v}$. Equation (22) is the von Neumann equation and can be solved analytically,

$$\hat{\eta}(t + \Delta t) = \hat{U} \hat{\eta}(t) \hat{U}^\dagger, \quad (23)$$

where $\hat{U} = \exp(i \frac{\hat{\boldsymbol{\mu}} \cdot \mathbf{B} \Delta t}{\hbar})$ is the propagator and Δt the time step size. For spin- $\frac{1}{2}$ particles, the components of spin operator \hat{s} in z basis are

$$\hat{s}_x = \frac{\hbar}{2} \begin{pmatrix} 0 & 1 \\ 1 & 0 \end{pmatrix}, \hat{s}_y = \frac{\hbar}{2} \begin{pmatrix} 0 & -i \\ i & 0 \end{pmatrix}, \hat{s}_z = \frac{\hbar}{2} \begin{pmatrix} 1 & 0 \\ 0 & -1 \end{pmatrix}, \quad (24)$$

and the propagator is

$$\hat{U} = \begin{pmatrix} \cos(\phi) + i \frac{B_z}{|\mathbf{B}|} \sin(\phi) & \frac{iB_x + B_y}{|\mathbf{B}|} \sin(\phi) \\ \frac{iB_x - B_y}{|\mathbf{B}|} \sin(\phi) & \cos(\phi) - i \frac{B_z}{|\mathbf{B}|} \sin(\phi) \end{pmatrix}, \quad (25)$$

where $\phi = \frac{\gamma |\mathbf{B}| \Delta t}{2}$. For spin-1 particles, the components of \hat{s} are

$$\hat{s}_x = \frac{\hbar}{\sqrt{2}} \begin{pmatrix} 0 & 1 & 0 \\ 1 & 0 & 1 \\ 0 & 1 & 0 \end{pmatrix}, \quad \hat{s}_y = \frac{\hbar}{\sqrt{2}} \begin{pmatrix} 0 & -i & 0 \\ i & 0 & -i \\ 0 & i & 0 \end{pmatrix},$$

$$\hat{s}_z = \hbar \begin{pmatrix} 1 & 0 & 0 \\ 0 & 0 & 0 \\ 0 & 0 & -1 \end{pmatrix}, \quad (26)$$

and the propagator is

$$\hat{U} = \begin{bmatrix} \hat{I} - \left(\frac{\hat{s}_x}{\hbar} \right)^2 (1 - \cos(\phi_x)) + i \left(\frac{\hat{s}_x}{\hbar} \right) \sin(\phi_x) \\ \cdot \left[\hat{I} - \left(\frac{\hat{s}_y}{\hbar} \right)^2 (1 - \cos(\phi_y)) + i \left(\frac{\hat{s}_y}{\hbar} \right) \sin(\phi_y) \right] \\ \cdot \left[\hat{I} - \left(\frac{\hat{s}_z}{\hbar} \right)^2 (1 - \cos(\phi_z)) + i \left(\frac{\hat{s}_z}{\hbar} \right) \sin(\phi_z) \right], \quad (27)$$

where \hat{I} is the identity matrix and $\phi_{\{x,y,z\}} = \gamma B_{\{x,y,z\}} \Delta t$. The analytical solution (23) ensures that the diagonal terms of $\hat{\eta}$ are bounded in $[0, 1]$, and the trace of $\hat{\eta}$ is one. The probability distribution for spin eigenstates can be obtained from diagonal terms of the density matrix. For tritons, the probabilities for spin eigenstates $m_z = \{\frac{1}{2}, -\frac{1}{2}\}$ are η_{00}^T and η_{11}^T , respectively. For deuterons, the probabilities for spin eigenstates $m_z = \{1, 0, -1\}$ are η_{00}^D, η_{11}^D , and η_{22}^D , respectively. The triton polarization in $+z$ direction is $p_z^T = \eta_{00}^T - \eta_{11}^T$. The vector polarization of deuteron is $p_z^D = \eta_{00}^D - \eta_{22}^D$ and the tensor polarization of deuteron is $p_{zz}^D = \eta_{00}^D - 2\eta_{11}^D + \eta_{22}^D$. The fusion reaction rate and neutron angular distributions can be obtained from the density matrices of DT. The fusion reactivity of DT reaction can be calculated as [1,2]

$$\langle \sigma v \rangle = \langle \sigma_0 v \rangle \left[\frac{3}{2} (\eta_{00}^T \eta_{00}^D + \eta_{11}^T \eta_{22}^D) + \eta_{11}^D + \frac{1}{2} (\eta_{00}^T \eta_{22}^D + \eta_{11}^T \eta_{00}^D) \right], \quad (28)$$

where $\langle \sigma_0 v \rangle$ is the unpolarized reactivity [35]. The fusion rate equation for equimolar DT fuel is

$$\frac{\partial n_n}{\partial t} = \langle \sigma v \rangle \left(\frac{\rho f}{m_D + m_T} \right)^2, \quad (29)$$

where n_n is neutron density, m_D and m_T are masses of DT, respectively. The angular distribution for neutrons is

$$\frac{\partial}{\partial t} \frac{\partial n_n}{\partial \Omega} = \frac{\langle \sigma_0 v \rangle}{4\pi} \left(\frac{\rho f}{m_D + m_T} \right)^2 \left[\frac{9}{4} (\eta_{00}^T \eta_{00}^D + \eta_{11}^T \eta_{22}^D) \sin^2 \theta + \frac{1}{4} (\eta_{00}^T \eta_{22}^D + \eta_{11}^T \eta_{00}^D + 2\eta_{11}^D) (3 \cos^2 \theta + 1) \right], \quad (30)$$

where θ is the polar angle. The angular distributions for neutrons with $m_z = \{\frac{1}{2}, -\frac{1}{2}\}$ are $\frac{\partial n_n^+}{\partial \Omega}$ and $\frac{\partial n_n^-}{\partial \Omega}$, respectively,

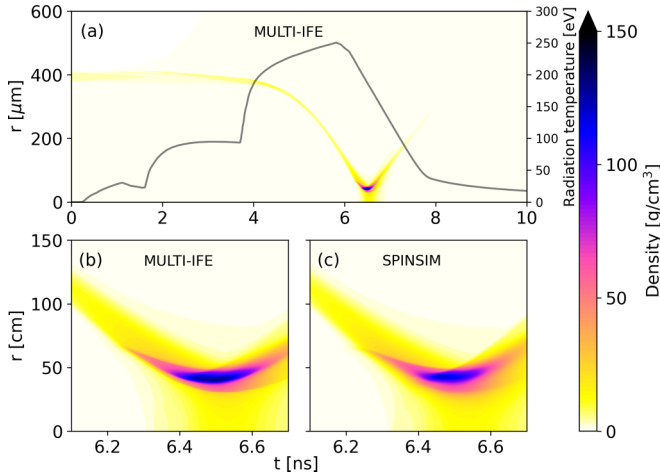


FIG. 1. (a) Target mass density evolution from MULTI-IFE simulations. The black solid line is the radiation profile used to drive the implosion. (b) MULTI-IFE simulation results of the stagnation phase. (c) SPINSIM simulation results of the stagnation phase.

satisfying $\frac{\partial n_n}{\partial \Omega} = \frac{\partial n_n^+}{\partial \Omega} + \frac{\partial n_n^-}{\partial \Omega}$ and

$$\begin{aligned} \frac{\partial}{\partial t} \left(\frac{\partial n_n^+}{\partial \Omega} - \frac{\partial n_n^-}{\partial \Omega} \right) &= \frac{\langle \sigma_0 v \rangle}{4\pi} \left(\frac{\rho f}{m_D + m_T} \right)^2 \\ &\times \left[\frac{9}{4} (\eta_{00}^T - \eta_{11}^T) (\eta_{00}^D - 2\eta_{11}^D + \eta_{22}^D) \sin^2 \theta \cos^2 \theta \right. \\ &- \frac{9}{4} (\eta_{00}^T \eta_{00}^D - \eta_{11}^T \eta_{22}^D) \sin^4 \theta + \frac{1}{4} (2\eta_{00}^T \eta_{11}^D - 2\eta_{11}^T \eta_{11}^D \\ &\left. + \eta_{11}^T \eta_{00}^D - \eta_{00}^T \eta_{22}^D) (3 \cos^2 \theta - 1)^2 \right]. \end{aligned} \quad (31)$$

Equations (29)–(31) are solved to obtain the neutron yield, neutron angular distribution and neutron polarization of polarized DT fusion. The numerical algorithms to solve the above equations on a graphics processing unit are developed and implemented in a 3D STHD simulation code SPINSIM [18].

III. SIMULATION RESULTS

The capsule-only 3D STHD simulations of polarized DT gas-filled target implosions are performed to study the persistence of fuel polarizations. The target capsule is made of a high density carbon (HDC) shell filled with highly polarized DT gas ($p_z^T = p_z^D = p_{zz}^D = 0.9$). Such high polarizations can be potentially achieved with the atomic beam sources [14,15]. The inner radius and thickness of the HDC ablator are 380 μm and 28 μm , respectively. The density of HDC is 3.52 g/cm^3 and the density of the DT gas is 9.282 mg/cm^3 . The initial temperature of the capsule is 65.65 K. Because the development of hydrodynamic instabilities, amplification of magnetic fields, and depolarization of the polarized fuels are during the stagnation phase of the implosion [21], only the stagnation phase is simulated with SPINSIM. The radiation hydrodynamics code MULTI-IFE [36] is used to provide the fluid quantities as input data for STHD simulations. As shown in Fig. 1(a), the capsule is ablated by radiations with peak

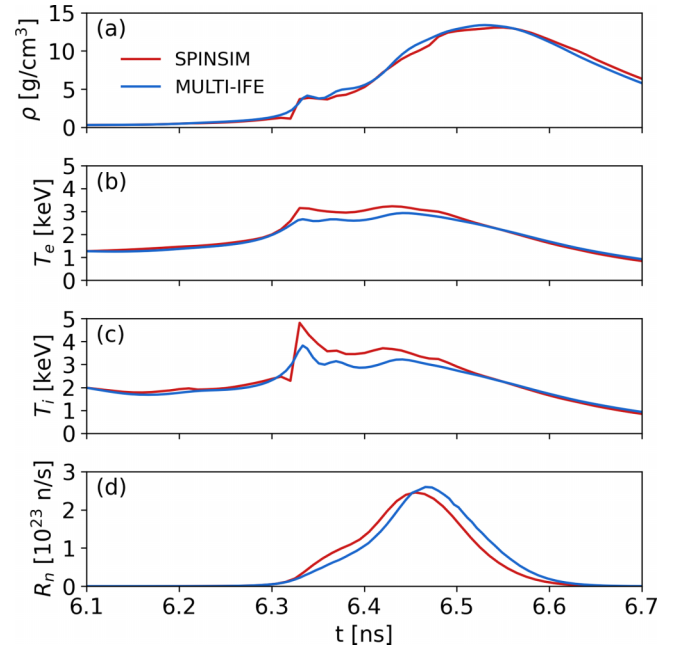


FIG. 2. Simulation results of polarized target implosion of SPINSIM and MULTI-IFE. (a) Density at fuel center, (b) electron temperature at fuel center, (c) ion temperature at fuel center, (d) neutron production rate.

temperature of about 250 eV, which can be generated by a 100 kJ level laser facility [37]. The hydrodynamic quantities ρ , v , T_i , T_e and radiation temperature T_{rad} at 6.1 ns from MULTI-IFE simulation are used as initial conditions for SPINSIM simulations. The simulation results of the stagnation phase of the implosion without perturbations from MULTI-IFE and SPINSIM are shown in Figs. 1(b) and 1(c). The SPINSIM simulation is carried out on 512^3 uniform grid cells, and the simulation domain size is $300^3 \mu\text{m}^3$. 20 radiation energy groups are used with energy range from 1 eV to 5 keV. Tabulated EOS and opacities are identical in the MULTI-IFE and SPINSIM simulations. The neutron yield of the MULTI-IFE simulation is 3.55×10^{13} , and the neutron yield of the SPINSIM simulation is 3.40×10^{13} , with a difference of about 4%. The alpha particle self-heating effects are neglected in both SPINSIM and MULTI-IFE simulations for the low-yield gas-filled target. The densities at fuel centers for SPINSIM and MULTI-IFE simulations are very close, as shown in Fig. 2(a). The electron temperature and ion temperature at the fuel center of SPINSIM are slightly larger than MULTI-IFE, as shown in Figs. 2(b) and 2(c). The peak neutron production rate is reached at about 6.45 ns (bang time) for SPINSIM, which is slightly ahead of MULTI-IFE, as shown in Fig. 2(d).

The polar mode-2 (P_2) perturbation which forms from low-mode radiation drive asymmetries [38,39] is added to the implosion velocity of STHD simulation. High-mode perturbations, which rise from the defects of the target, are also added with 128 RTI spikes and bubbles with random positions and amplitudes. The fuel density distribution at bang time of the simulation with only P_2 perturbation is shown in Fig. 3(a), and the result with both P_2 perturbation and high-mode perturbation is shown in Fig. 3(b). The low-mode polar asymmetries

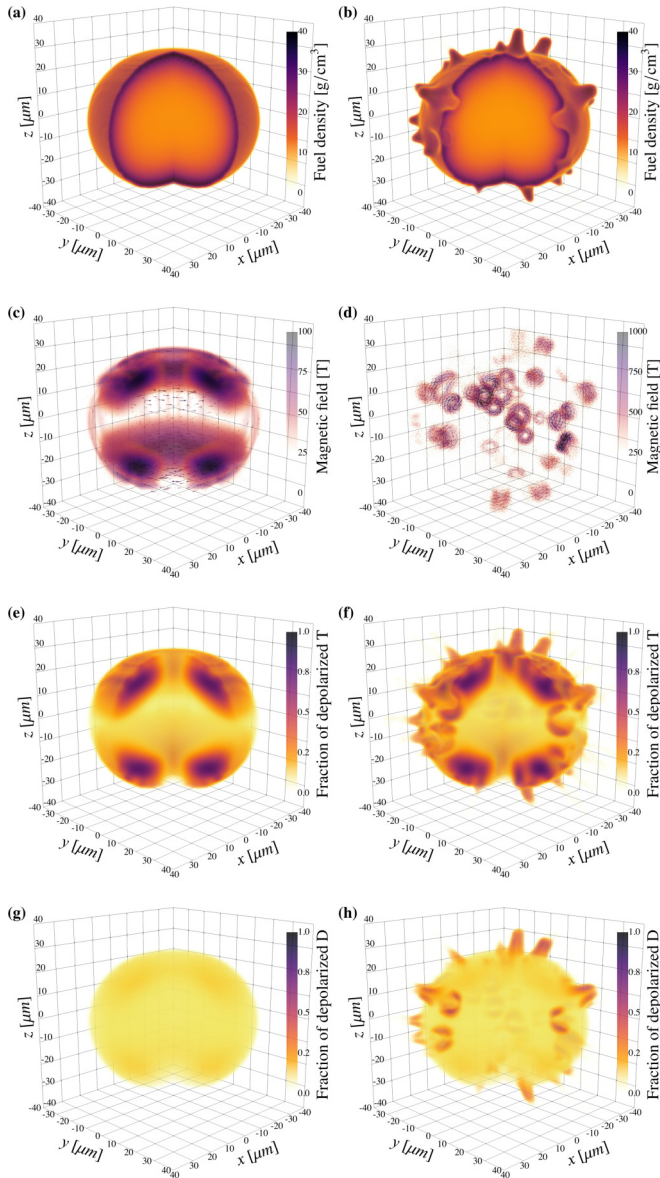


FIG. 3. 3D STHD simulation results at bang time. (a), (b) Fuel densities, (c), (d) magnetic fields, (e), (f) fraction of depolarized tritons (η_{11}^T), (g), (h) fraction of depolarized deuterons ($\eta_{11}^D + \eta_{22}^D$). (a), (c), (e), and (g) are simulation results with only low-mode asymmetry. (b), (d), (f), and (h) are simulation results with low-mode asymmetry and high-mode perturbations. The data in $x, y > 0$ region are set to be transparent except for (d).

can be modeled using Legendre modes [38],

$$R(\theta) = R_0 \left(1 + a_l \sqrt{\frac{2l+1}{4\pi}} P_l(\cos\theta) \right), \quad (32)$$

where R is the fuel outer radius, R_0 is the unperturbed radius, P_l is the Legendre polynomial of order l , and a_l is the fractional asymmetry amplitude, which is also referred to as P_l/P_0 . For Figs. 3(a) and 3(b), the amplitude of the perturbation at bang time is $P_2/P_0 = -0.206$, indicating that the fuel is oblate. RTI spikes and bubbles are developed near the fuel-ablator interface as shown in Fig. 3(b). The magnetic fields for simulations with and without high-mode

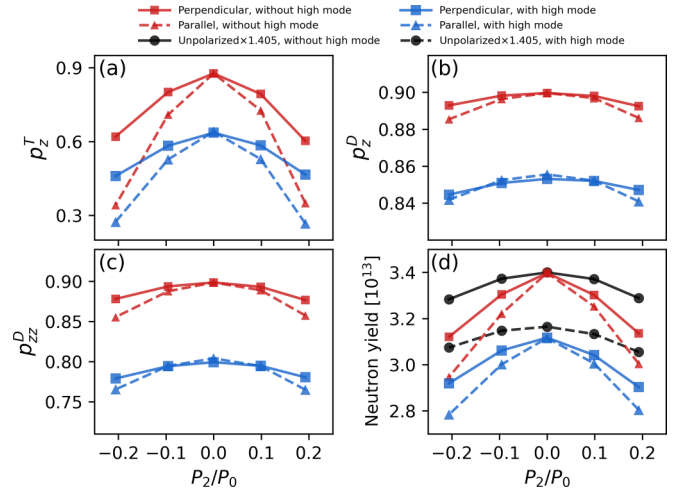


FIG. 4. (a) Triton polarizations p_z^T , (b) deuteron vector polarizations p_z^D , (c) deuteron tensor polarizations p_z^{Dz} , and (d) neutron yields for different P_2 perturbation amplitudes. The fuel polarizations are simulation results at bang time. Each marker stands for a simulation run. For the polarized cases, the initial fuel polarizations are $p_z^T = p_z^D = p_z^{Dz} = 0.9$. For the unpolarized cases, the initial fuel polarizations are $p_z^T = p_z^D = p_z^{Dz} = 0$.

perturbations are depicted in Figs. 3(c) and 3(d), respectively. The axis of polar asymmetry, which is typically the axis of the hohlraum, is along the z direction. The magnetic fields generated by low-mode polar asymmetry are in the order of 100 T and the directions are mainly azimuthal, as shown in Fig. 3(c). The magnetic fields generated by high-mode perturbations are in the order of 1000 T and are circling around RTI spikes and bubbles, as shown in Fig. 3(d). Though the amplitudes of low-mode magnetic fields are smaller than those of high-mode magnetic fields, the volume of tritons affected by the low-mode magnetic fields is much larger, as shown in Figs. 3(e) and 3(f). Due to the smaller gyromagnetic ratio, deuterons are less affected by the low-mode magnetic fields, as shown in Figs. 3(e) and 3(f). But the high-mode magnetic fields are strong enough to depolarize deuterons, as shown in Fig. 3(f). The initial spins of the DT fuel are aligned along the z axis, parallel to the axis of hohlraum. This indicates that the initial spins of the DT fuel are perpendicular to the low-mode magnetic fields and the depolarization happens everywhere the low-mode magnetic fields are present.

To address the large volume depolarization by the low-mode magnetic fields, the spin alignment of the polarized DT fuels can be optimized. The depolarization of DT ions can be reduced if the initial spins of DT fuel are aligned perpendicular to the axis of hohlraum. Figures 4(a)–4(c) show the fuel depolarizations at bang time for different P_2 perturbation amplitudes. The fuel polarizations decrease with the increment of the absolute values of P_2 amplitudes. The triton polarizations for the perpendicular cases are larger than those for the parallel cases as depicted in Fig. 4(a). The triton polarizations are smaller than the deuteron polarizations, as shown in Figs. 4(a) and 4(b). The deuteron polarizations are more sensitive to high-mode perturbations as shown in Figs. 4(b) and 4(c). The neutron yields decrease with the increasing of absolute values of P_2 perturbation amplitudes, as shown in

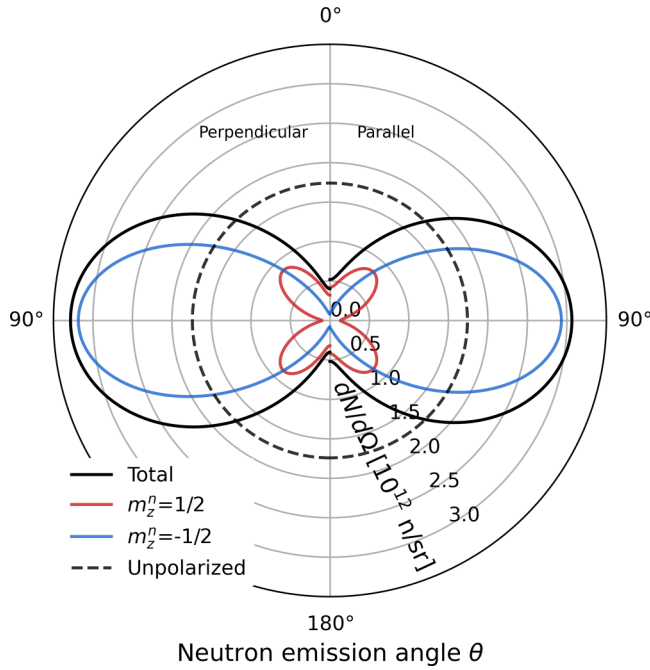


FIG. 5. Neutron angular distributions for polarized DT gas-filled capsule implosions with perpendicular spin alignment (left) and parallel spin alignment (right). The dashed line shows the result of unpolarized fuels.

Fig. 4(d). For the initial fuel polarizations $p_z^T = p_z^D = p_{zz}^D = 0.9$, the neutron yield is 40.5% higher than the unpolarized case when no perturbations are present. The yield degradation due to P_2 perturbations is more severe for the polarized cases than the unpolarized cases. And the yield degradation for the perpendicularly polarized cases is less severe than the parallel polarized cases. When $P_2/P_0 = -0.206$, the neutron yield for the parallel case is about 26.5% higher than the unpolarized case and for the perpendicular case, the yield enhancement is about 33.5%. Figure 5 shows the neutron angular distributions of polarized cases with perpendicular spin alignment and parallel spin alignment as well as the unpolarized case (the $P_2/P_0 = -0.206$ and high-mode perturbations are present). For the unpolarized case, the neutron angular distribution is isotropic and the differential yield is

$dN/d\Omega = 1.74 \times 10^{12}$ n/sr. For the polarized case, the neutron emissions are anisotropic and peaked at equator ($\theta = 90^\circ$). The neutrons emitted at equator are mostly in spin state $m_z^n = -\frac{1}{2}$. For the perpendicular case, the peak differential yield is 3.28×10^{12} n/sr, which is 88.6% higher than the unpolarized case and 7.2% higher than the parallel case. The simulation results show that the perpendicular spin alignment can reduce the depolarization of DT ions and enhance the neutron yields. The neutron signals can be used in experiments as diagnostics of fuel polarization persistence.

IV. DISCUSSIONS

The persistence of spin-polarized DT fuels in indirectly driven ICF implosions are investigated with 3D STHD simulations. The spin transport equation is derived using the density matrix formalism to model the spin dynamics of spin- $\frac{1}{2}$ and spin-1 particles. The spin transport equations are solved self-consistently in STHD simulations. The simulation results show that triton polarizations are sensitive to large scale magnetic fields generated by polar mode asymmetries. The depolarization of tritons can be reduced when the spins of the fuel are aligned perpendicular to the axis of hohlraum. The solutions of spin transport equations can be used in fusion rate equations to obtain the neutron yield and neutron angular distribution. The neutron signals can be used in experiments as diagnostics of fuel polarization persistence. For the cryogenic DT target with MJ laser energy used for ignition [10,11], stronger self-generated magnetic fields [21] can be generated than the low-yield gas-filled target with 100 kJ laser energy investigated in this paper. The depolarization of DT ions can be more severe. Further work is required to investigate whether the spin polarized fuel could contribute to ignition in the cryogenic DT target implosion.

ACKNOWLEDGMENT

This work was supported by the National Natural Science Foundation of China (Grant No. 12105193) and Fundamental Research Funds for the Central Universities (Grant No. 2021SCU12119).

[1] R. Kulsrud, H. Furth, E. Valeo, and M. Goldhaber, Fusion Reactor Plasmas with Polarized Nuclei, *Phys. Rev. Lett.* **49**, 1248 (1982).
 [2] R. Kulsrud, E. Valeo, and S. Cowley, Physics of spin-polarized plasmas, *Nucl. Fusion* **26**, 1443 (1986).
 [3] R. M. More, Nuclear Spin-Polarized Fuel in Inertial Fusion, *Phys. Rev. Lett.* **51**, 396 (1983).
 [4] B. Coppi, F. Pegoraro, and J. J. Ramos, Instability of Fusing Plasmas and Spin-Depolarization Processes, *Phys. Rev. Lett.* **51**, 892 (1983).
 [5] B. Coppi, S. Cowley, R. Kulsrud, P. Detragiache, and F. Pegoraro, High-energy components and collective modes in thermonuclear plasmas, *Phys. Fluids* **29**, 4060 (1986).

[6] J.-P. Didelez and C. Deutsch, Persistence of the polarization in a fusion process, *Laser Part. Beams* **29**, 169 (2011).
 [7] G. Ciullo, R. Engels, M. Büscher, and A. Vasilyev, *Nuclear Fusion with Polarized Fuel* (Springer, Cham, 2016).
 [8] G. Hupin, S. Quaglioni, and P. Navrátil, *Ab initio* predictions for polarized deuterium-tritium thermonuclear fusion, *Nat. Commun.* **10**, 351 (2019).
 [9] C. N. Danson and L. A. Gizzi, Inertial confinement fusion ignition achieved at the national ignition facility—an editorial, *High Power Laser Sci. Eng.* **11**, e40 (2023).
 [10] A. B. Zylstra, O. A. Hurricane, D. A. Callahan, A. L. Kritcher, J. E. Ralph, H. F. Robey, J. S. Ross, C. V. Young, K. L. Baker, D. T. Casey *et al.*, Burning plasma achieved in inertial fusion, *Nature (London)* **601**, 542 (2022).

- [11] H. Abu-Shawareb, R. Acree, P. Adams, J. Adams, B. Addis, R. Aden, P. Adrian, B. B. Afeyan, M. Aggleton, L. Aghaian *et al.* (Indirect Drive ICF Collaboration), Lawson Criterion for Ignition Exceeded in an Inertial Fusion Experiment, *Phys. Rev. Lett.* **129**, 075001 (2022).
- [12] M. Temporal, V. Brandon, B. Canaud, J. Didelez, R. Fedosejevs, and R. Ramis, Ignition conditions for inertial confinement fusion targets with a nuclear spin-polarized DT fuel, *Nucl. Fusion* **52**, 103011 (2012).
- [13] Y. Pan and S. Hatchett, Spin-polarized fuel in high gain ICF targets, *Nucl. Fusion* **27**, 815 (1987).
- [14] A. Roberts, P. Elmer, M. Ross, T. Wise, and W. Haeberli, Medium field rf transitions for polarized beams of hydrogen and deuterium, *Nucl. Instr. Meth. Phys. Res. A* **322**, 6 (1992).
- [15] C. Baumgarten, B. Braun, V. Carassiti, G. Ciullo, G. Court, P. Dalpiaz, E. Garutti, A. Golendukhin, G. Graw, W. Haeberli *et al.*, The storage cell of the polarized H/D internal gas target of the HERMES experiment at HERA, *Nucl. Instr. Meth. Phys. Res. A* **496**, 277 (2003).
- [16] R. Engels, M. Gaißer, R. Gorski, K. Grigoryev, M. Mikirtychyants, A. Nass, F. Rathmann, H. Seyfarth, H. Ströher, P. Weiss *et al.*, Production of hyperpolarized h_2 molecules from $\bar{\text{h}}$ atoms in gas-storage cells, *Phys. Rev. Lett.* **115**, 113007 (2015).
- [17] B. Goel and W. Heeringa, Spin polarized ICF targets, *Nucl. Fusion* **28**, 355 (1988).
- [18] R. Hu, H. Zhou, Z. Tao, M. Lv, S. Zou, and Y. Ding, Spin depolarization induced by self-generated magnetic fields during cylindrical implosions, *Phys. Rev. E* **102**, 043215 (2020).
- [19] M. J.-E. Manuel, C. K. Li, F. H. Séguin, J. Frenje, D. T. Casey, R. D. Petrasso, S. X. Hu, R. Betti, J. D. Hager, D. D. Meyerhofer, and V. A. Smalyuk, First Measurements of Rayleigh-Taylor-Induced Magnetic Fields in Laser-Produced Plasmas, *Phys. Rev. Lett.* **108**, 255006 (2012).
- [20] B. Srinivasan, G. Dimonte, and X.-Z. Tang, Magnetic field generation in Rayleigh-Taylor unstable inertial confinement fusion plasmas, *Phys. Rev. Lett.* **108**, 165002 (2012).
- [21] C. A. Walsh, J. P. Chittenden, K. McGlinchey, N. P. L. Niasse, and B. D. Appelbe, Self-Generated Magnetic Fields in the Stagnation Phase of Indirect-Drive Implosions on the National Ignition Facility, *Phys. Rev. Lett.* **118**, 155001 (2017).
- [22] Z. Gong, Y. Shou, Y. Tang, and X. Yan, Energetic spin-polarized proton beams from two-stage coherent acceleration in laser-driven plasma, *Phys. Rev. E* **102**, 053212 (2020).
- [23] Z. Gong, K. Z. Hatsagortsyan, and C. H. Keitel, Retrieving Transient Magnetic Fields of Ultrarelativistic Laser Plasma via Ejected Electron Polarization, *Phys. Rev. Lett.* **127**, 165002 (2021).
- [24] Z. Gong, K. Z. Hatsagortsyan, and C. H. Keitel, Deciphering in situ electron dynamics of ultrarelativistic plasma via polarization pattern of emitted γ -photons, *Phys. Rev. Res.* **4**, L022024 (2022).
- [25] Z. Gong, K. Z. Hatsagortsyan, and C. H. Keitel, Electron Polarization in Ultrarelativistic Plasma Current Filamentation Instabilities, *Phys. Rev. Lett.* **130**, 015101 (2023).
- [26] M. Marklund and G. Brodin, Dynamics of spin- $\frac{1}{2}$ quantum plasmas, *Phys. Rev. Lett.* **98**, 025001 (2007).
- [27] D. S. Clark, C. R. Weber, J. L. Milovich, J. D. Salmonson, A. L. Kritcher, S. W. Haan, B. A. Hammel, D. E. Hinkel, O. A. Hurricane, O. S. Jones *et al.*, Three-dimensional simulations of low foot and high foot implosion experiments on the national ignition facility, *Phys. Plasmas* **23**, 056302 (2016).
- [28] S. C. Cowley, R. M. Kulsrud, and E. Valeo, A kinetic equation for spin-polarized plasmas, *Phys. Fluids* **29**, 430 (1986).
- [29] W. Y. Zhang and R. Balescu, Statistical mechanics of a spin-polarized plasma, *J. Plasma Phys.* **40**, 199 (1988).
- [30] R. Balescu and W. Y. Zhang, Kinetic equation, spin hydrodynamics and collisional depolarization rate in a spin-polarized plasma, *J. Plasma Phys.* **40**, 215 (1988).
- [31] R. Hu, H. Zhou, Z. Tao, Z. Zhang, M. Lv, S. Zou, and Y. Ding, Spin transport hydrodynamics of polarized deuterium-tritium fusion plasma, [arXiv:2204.11523](https://arxiv.org/abs/2204.11523).
- [32] E. F. Toro, *Riemann Solvers and Numerical Methods for Fluid Dynamics* (Springer, Berlin, Heidelberg, 2009).
- [33] S. I. Braginskii, Transport processes in a plasma, *Rev. Plasma Phys.* **1**, 205 (1965).
- [34] E. M. Epperlein and M. G. Haines, Plasma transport coefficients in a magnetic field by direct numerical solution of the Fokker-Planck equation, *Phys. Fluids* **29**, 1029 (1986).
- [35] H.-S. Bosch and G. Hale, Improved formulas for fusion cross-sections and thermal reactivities, *Nucl. Fusion* **32**, 611 (1992).
- [36] R. Ramis and J. Meyer-ter-Vehn, MULTI-IFE-a one-dimensional computer code for inertial fusion energy (IFE) target simulations, *Comput. Phys. Commun.* **203**, 226 (2016).
- [37] X. Xie, C. Wu, J. Chen, S. Liu, L. Hou, H. Du, H. Cai, L. Guo, K. Ren, Z. Li *et al.*, Characterization of radiation drive by measuring the localized re-emitted flux from the capsule in inertial confinement fusion experiments, *Nucl. Fusion* **62**, 126008 (2022).
- [38] A. B. Zylstra, J. A. Frenje, F. H. Séguin, J. R. Rygg, A. Kritcher, M. J. Rosenberg, H. G. Rinderknecht, D. G. Hicks, S. Friedrich, R. Bionta *et al.*, In-flight observations of low-mode ρ R asymmetries in NIF implosions, *Phys. Plasmas* **22**, 056301 (2015).
- [39] C. Li, F. Ge, C. Wu, J. Gu, Z. Chen, Z. Dai, X. Li, T. Huang, B. Chen, B. Deng *et al.*, Investigations on the P2 drive asymmetry and its effect on the shell asymmetry in a symmetry tuning experiment at the 100 kJ laser facility, *Phys. Plasmas* **28**, 112707 (2021).